

Supplementary Information

Effect of strain on effective Duffing nonlinearity in CVD-MoS₂ resonator

Chandan Samanta¹, Nishta Arora¹, V. Kranthi Kumar¹, Sinivasan Raghavan^{1,2} and A. K. Naik^{1*}

¹Centre for Nano Science and Engineering, Indian Institute of Science, Bangalore, 560012, India

²Materials Research Centre, Indian Institute of Science, Bangalore 560012, India

*corresponding Author: anaik@cense.iisc.ernet.in

A. CVD growth of MoS₂ films:

The growth of MoS₂ is carried out in a custom-built horizontal, hot-wall chemical vapour deposition (CVD) reactor with Mo(CO)₆ powder placed in a vaporizer and heated to a temperature of 100°C. The Mo vapours are carried into the reactor using H₂ and H₂S gases. The H₂S gas is used as a precursor for sulphur (S). The H₂ gas is also used as a dilution gas. All the precursors enter the reactor in the gas phase through separate lines. Highly p-doped Si substrates having a 285nm thick SiO₂ layer on top are used as a substrate for growth. The substrates are cleaned sequentially in acetone, isopropyl alcohol (IPA) and deionized water in an ultrasonic bath for 5 minutes each and dried with a N₂ blow dryer.

The growth is carried out at a temperature of 850°C and the reactor pressure of 600 Torr. Prior to deposition, the reactor is pumped down to the desired pressure, and the temperature is ramped at 25°C/minute to 850°C while keeping H₂ gas with a flow rate of 1000 sccm. The growth is carried out for 45 seconds. The Mo(CO)₆ powder in the vaporizer is heated at 100°C and

maintained at a pressure of 18 psi, with a carrier gas flow of 18 sccm. The ratio of gas flow rates, Mo: H₂S: H₂, is maintained at 1:10:1000. The details of growth can be found somewhere else¹.

B. Raman characterization:

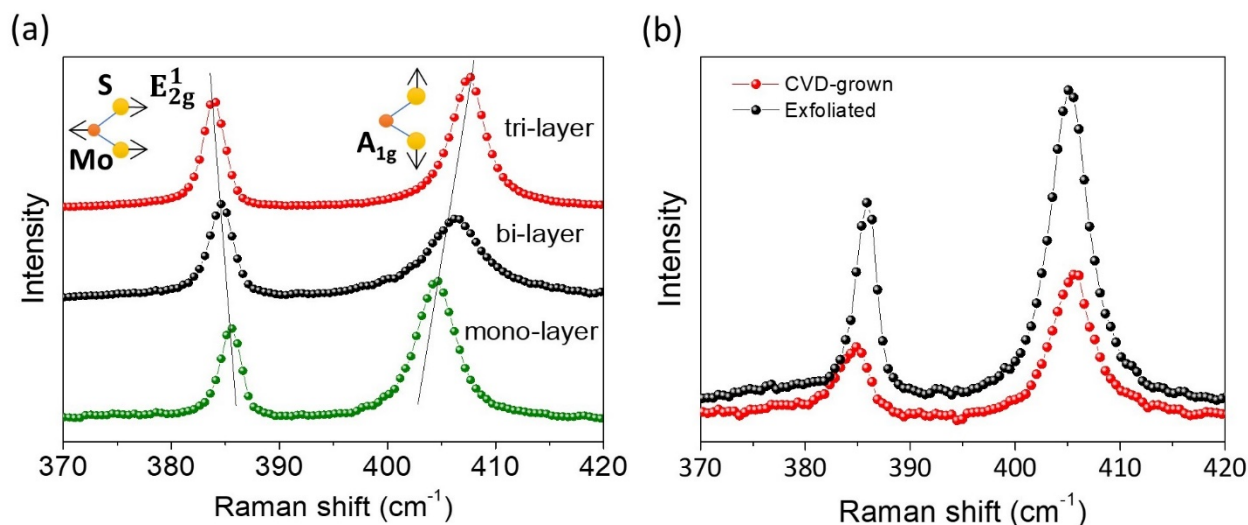


Figure S1: (a) Raman spectrum of mono, bi and tri-layered MoS₂ obtained using 532 nm laser wavelength. (b) Comparison of Raman spectrum of exfoliated and CVD grown mono layered MoS₂.

Raman spectroscopy is carried out on exfoliated and CVD grown MoS₂ layers to determine their layer numbers². The prominent peaks obtained are the E_{2g}¹ and A_{1g} peaks. The difference in their relative positions is used to determine the number of layers of MoS₂. The spectra are obtained using 532 nm laser wavelength. The intensity of the laser is kept low enough (0.2 mW) to avoid heating effect during the measurements. Figure S1(a) shows the Raman spectrum of mono, bi and tri layer MoS₂ obtained using exfoliation. The peak separation for mono, bi and tri layer MoS₂ are around 17-19cm⁻¹, 20-22cm⁻¹ and 23cm⁻² respectively. Figure S1(b) depicts the comparison

between the Raman spectrum of mono-layer MoS₂ obtained using exfoliation and CVD growth. It confirms our ability to grow high quality MoS₂ crystalline film in CVD.

C. Electrical characterization:

It is well known from previously reported photoluminescence measurements that physisorbed O₂ and H₂O molecules on the MoS₂ surface affect charge carrier density significantly^{3,4}. Therefore, we study the effect of heating on the MoS₂ devices (both suspended and on-substrate devices) with an objective to improve the quality of the device. We mount the devices on the sample holder and keep the sample holder on top of the sample stage of the heater. Electrical characterizations of MoS₂ devices are carried out under high vacuum. The measurements are done by applying a DC voltage (V_{ds}) at the source electrode from Keithley source-meter while grounding the drain electrode. Another DC voltage (V_g^{DC}) is applied from a second Keithley source-meter to the Si substrate, which acts as a global back gate electrode in our device configuration.

Effect of heating on not-suspended (on-substrate) devices from exfoliated mono-layer

MoS₂ flake: At first, we carry out electrical measurements before we start heating. Figure S2(a) shows the output characteristic ($I_{ds} - V_{ds}$) of an on-substrate device fabricated from mono-layer MoS₂ flake at $V_g^{DC} = 0$. The asymmetric nature of ($I_{ds} - V_{ds}$) indicates that the contacts are not ohmic in the operating range of V_{ds} ($-0.5V$ to $+0.5V$). Figure S2(b) shows transfer characteristic ($I_{ds} - V_g^{DC}$) of the device while keeping $V_{ds} = 0.1V$. This depicts the n-type behaviour of exfoliated MoS₂ flakes. The transconductance $\left(\frac{dI_{ds}}{dV_g^{DC}}\right)$ and the field effect mobility (μ_{FE}) of the device are 3.5×10^{-8} and $\sim 20 \text{ cm}^2V^{-1}s^{-1}$ respectively. The mobility is extracted using the

expression: $\mu_{FE} = \frac{L}{WCV_{ds}} \frac{dI_{ds}}{dV_g^{DC}}$, where L and W are the channel length and width respectively

and C is the capacitance per unit area between the channel and back gate. The threshold

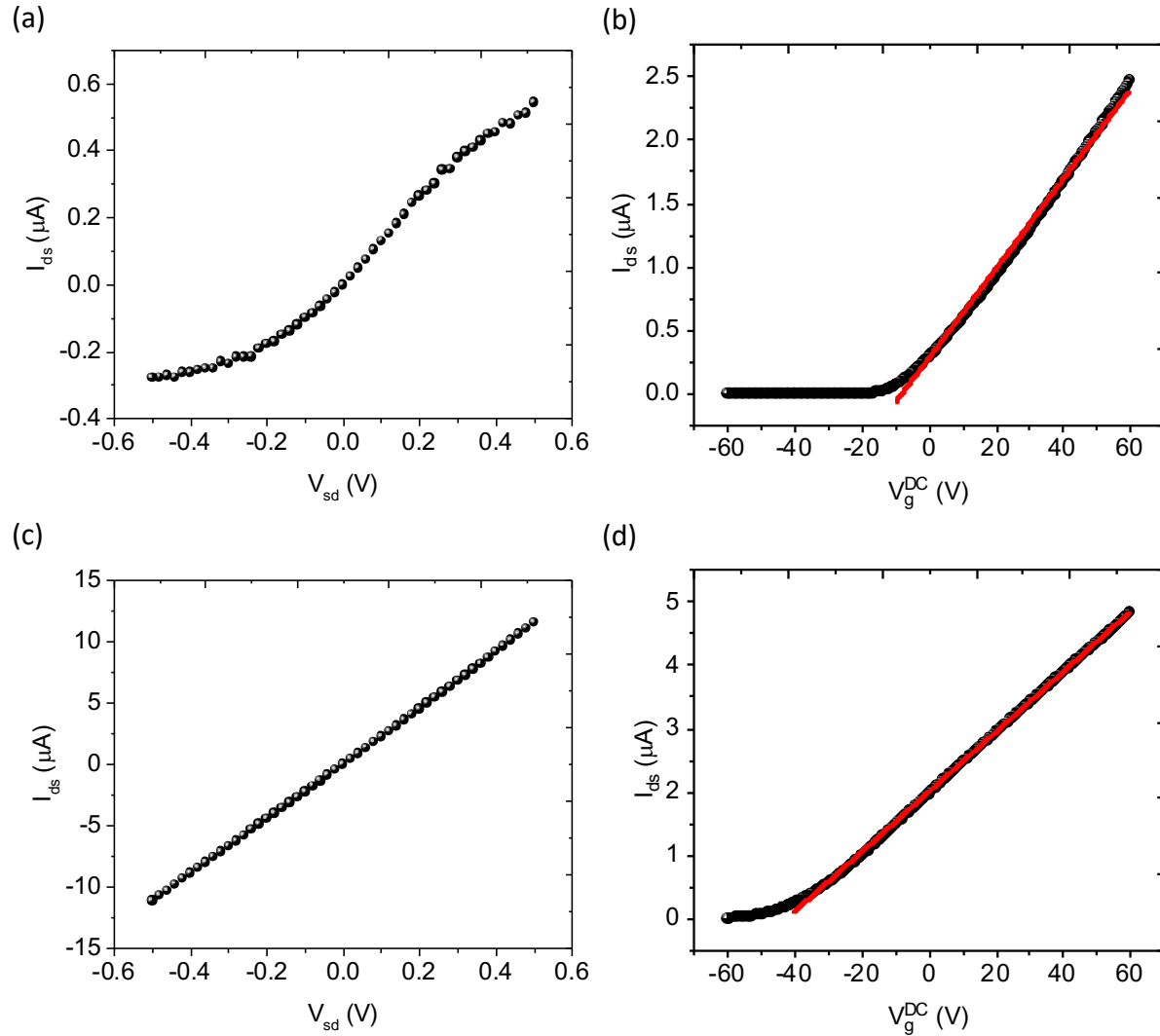


Figure S2: Effect of heating on electrical characterization of an on-substrate device form exfoliated mono-layer MoS₂. (a) Output characteristic before heating. (b) Transfer characteristic before heating. (c) Output characteristic after heating. (d) Transfer characteristic after heating. Red lines are linear fit to the transfer characteristics and are used for extracting transconductance.

voltage of this field effect transistor is around $V_g^{DC} = -5V$. Then, temperature of the sample stage is increased to 400K, and maintained for six hours approximately. After that, electrical measurements are carried out once the temperature reaches the room temperature. Figure S2(c) shows the output characteristic ($I_{ds} - V_{ds}$) of the device after heating at $V_g^{DC} = 0$. The symmetric nature of ($I_{ds} - V_{ds}$) indicates that the contacts are ohmic in the operating range of V_{ds} . The resistance of the device also improves from $1.8M\Omega$ to $45.1k\Omega$ at $V_{ds} = -0.5V$. However, we do not observe saturation of I_{ds} in the output characteristic for the range of $V_{ds} = \pm 0.5V$. Unfortunately, we never applied V_{ds} beyond $\pm 0.5V$ to observe saturation of I_{ds} . Figure S2(d) shows transfer characteristic ($I_{ds} - V_g^{DC}$) of the device while keeping $V_{ds} = 0.1V$. The transconductance improves from $3.5 \times 10^{-8} \Omega^{-1}$ to $4.7 \times 10^{-8} \Omega^{-1}$, and more interestingly threshold voltage now gets shifted from $V_g^{DC} \approx -5V$ to $V_g^{DC} \approx -45V$. It looks like from the above results that the heating improves the device performance in two ways: (i) makes the contacts ohmic (symmetric nature of the output characteristic), (ii) removes the adsorbents from the channel (shift in threshold voltage).

Effect of heating on suspended devices from exfoliated mono-layer MoS₂ flake: While suspending the membrane, BOE quickly propagates under MoS₂ and etches out the complete area under the flake. This process modifies the contact between the membrane and the metal considerably. As a result, for most of the devices, resistance increases significantly, and mobility degrades. However, the heating process as described previously helps to improve the quality of the device. Both the contact resistance and the transconductance improve significantly after heating. S3 shows the comparison between transfer characteristics of the device before and after heating. The contact resistance improves from $170M\Omega$ to $173k\Omega$ at $V_g^{DC} = 0$. Another

important aspect of heating is that transconductance becomes constant throughout the gate voltage of our interest ($V_g^{DC} = -12 \text{ V to } +12 \text{ V}$). The conductance improves from $3.1 \times 10^{-10} \Omega^{-1}$ (for positive V_g^{DC}) to $3.8 \times 10^{-9} \Omega^{-1}$. These improvements in electrical characteristics are crucial for electrical readout of the resonator and to estimate its mechanical parameters with accuracy. One important point to notice is that for the suspended device, transfer characteristic does not show off state after heating. This is because the transfer characteristic of the suspended devices is limited to a restricted range to avoid the collapse of the flake on the trench. The off state after heating for an on-substrate device is observed typically at much negative gate voltage (see figure S2(d)) than the range used for the suspended device.

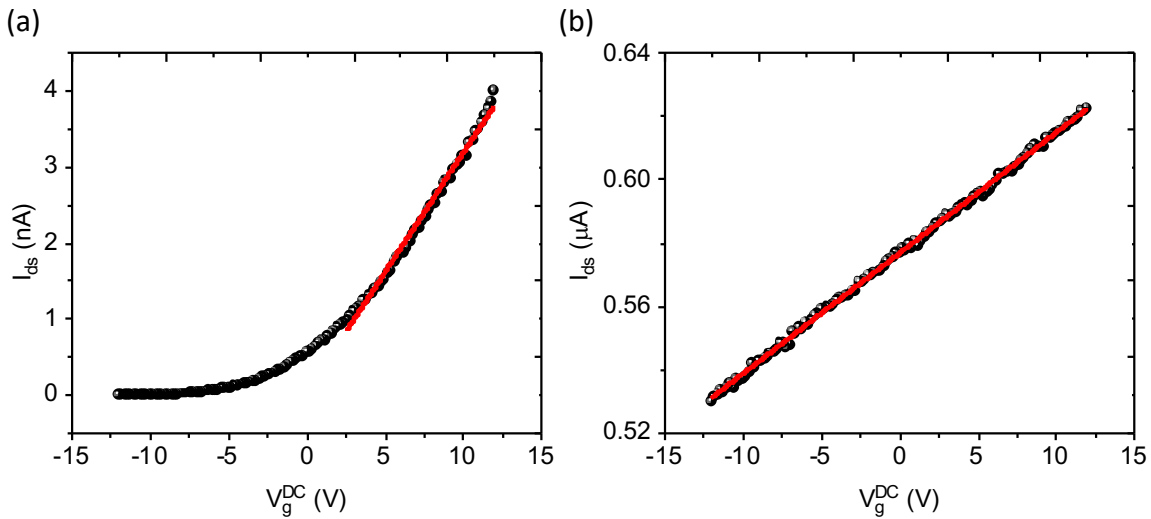


Figure S3: Effect of heating on the transfer characteristic of a suspended device from exfoliated monolayer MoS_2 device. (a) before heating, (b) after heating. Red lines are linear fit to the transfer characteristics and are used for extracting transconductance.

Comparison between suspended devices fabricated from exfoliated and CVD grown mono-layer MoS₂: We carry out same treatment for the devices fabricated from CVD grown mono-layer MoS₂. Then we compare electrical characteristics between exfoliated and CVD grown MoS₂ devices. Figure S4(a) shows the output characteristic and transfer characteristic obtained from exfoliated mono-layer MoS₂ device. The linear and symmetric nature of output characteristic shows that the contacts are ohmic in nature for V_{ds} from -0.5V to 0.5V. Two-probe resistance of the device is about 58k Ω which is the lowest reported till date, and the extracted

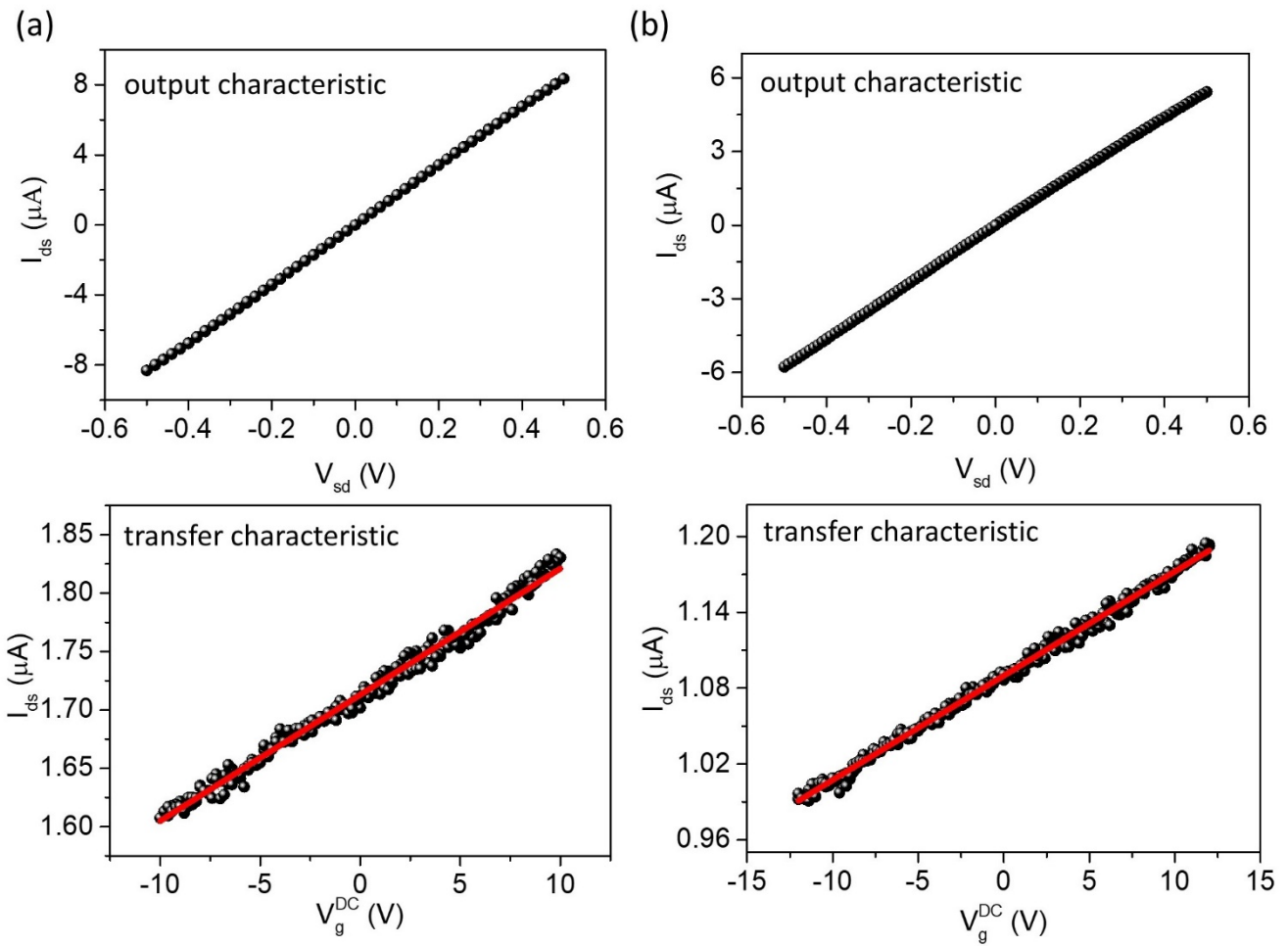


Figure S4: (a) Output and transfer characteristics of a device fabricated from exfoliated mono-layer flake. (b) Output and transfer characteristics of a device fabricated from CVD grown mono-layer flake. The red lines are linear fit to the transfer characteristics and are used for extracting mobility. For the transfer characteristic, $V_{ds} = 0.1V$ is used.

mobility of about $35 \text{ cm}^2\text{V}^{-1}\text{s}^{-1}$ is the highest reported value for suspended monolayer device till now. Figure S4(b) depicts the output characteristics and transfer characteristic obtained from CVD grown mono-layer MoS_2 device. The output characteristic of the device is linear and symmetric. Two probe resistance of the device is $70 \text{ k}\Omega$ and extracted field effect mobility is about $34 \text{ cm}^2\text{V}^{-1}\text{s}^{-1}$. This result clearly demonstrates that quality of CVD grown MoS_2 is as good as exfoliated MoS_2 flake.

Statistics: Figure S5 shows two-probe resistances and corresponding mobilities of few suspended devices fabricated from both exfoliated MoS_2 and CVD grown MoS_2 . The mobility of the devices is typically $15\text{-}40 \text{ cm}^2\text{V}^{-1}\text{s}^{-1}$. Two-probe resistances of suspended devices have been achieved as low as $58 \text{ k}\Omega$ and $30 \text{ k}\Omega$ for monolayer and few layers respectively.

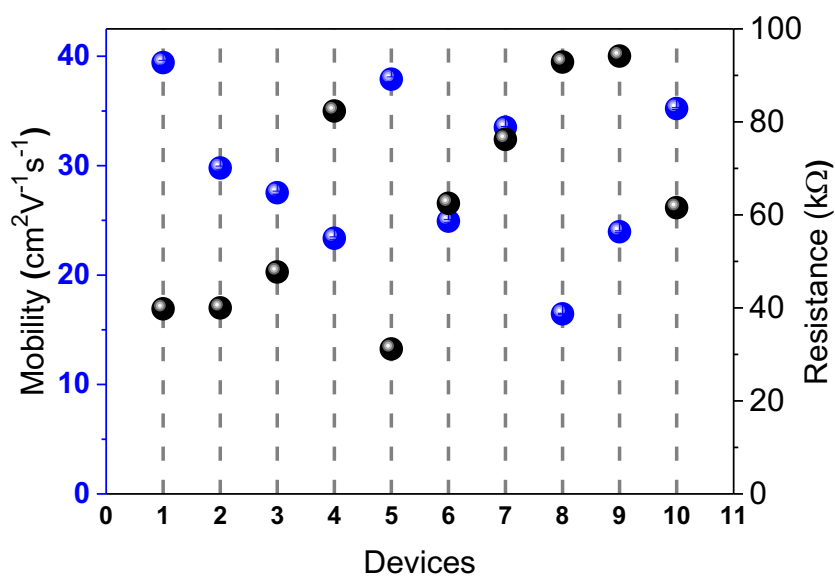


Figure S5: Mobility and corresponding resistance values of 10 suspended devices.

D. Electro-mechanical characterization:

One of the significant advantages of NEMS based on CNTs, Graphene and layered semiconductor materials like dichalcogenides is that the conductance of these materials depends on the charge induced by the gate voltage. This can be used to transduce mechanical motion into a time-varying current. The conductance of the resonator can be modulated through either C_g or V_g as induced charge follows: $q = C_g V_g$ (parallel plate approximation). We can write down the conductance as⁵

$$\tilde{G} = \frac{dG}{dq} \tilde{q},$$

where $\tilde{q} = \tilde{C}_g V_g^{\text{DC}} + C_g \tilde{V}_g$. The capacitance \tilde{C}_g is determined by the gap between the resonator and the gate. Then, modulation in the capacitance due to the oscillation of the resonator can be written as

$$\tilde{C}_g = \frac{dC_g}{dz} z(\omega).$$

Therefore, total modulation in the conductance can be written as

$$\tilde{G} = \frac{dG}{dq} \left(V_g^{\text{DC}} \frac{dC_g}{dz} z(\omega) + C_g \tilde{V}_g \right).$$

It's clear from the above equation that the conduction is modulated with the driving frequency, and directly proportional to the amplitude of the displacement of the resonator. Now, as the driving frequency approaches to the natural frequency of the resonator, the amplitude of the displacement gains its maximum value. At this point, modulation in conduction also gains its

maximum value. It is possible to measure this conduction modulation by directly measuring the RF current as described elsewhere^{6,7}.

Due to the global back gate configuration (i.e. the entire doped silicon substrate is used as the gate), typical parasitic capacitance between contact pads (source and drain contact pads) and the gate electrode is very high ($C_{\text{pad}} \sim 5\text{pF}$) in the devices. Typical resistance (R_{sd}) of a MoS₂ resonator varies from about 50k Ω to 1M Ω . The resonator, thus, act as a low pass filter and the cut off frequency can be estimated from

$$f_{\text{cutoff}} = \frac{1}{2\pi R_{\text{sd}} C_{\text{pad}}}.$$

For a device with a resistance of 1M Ω , the cutoff frequency is $\sim 1\text{MHz}$, which is much smaller than the resonant frequency of a typical resonator. As a result, direct measurement is not possible with this configuration. To overcome this problem, techniques have been implemented to mix down the signal frequency below the cutoff frequency of the resonator for detecting its motion. We utilize non-zero transconductance of the MoS₂ to use it as a frequency mixer. However, we compromise the detection rate by mixing down the signal frequency.

In 1ω mixed-down technique, a radio frequency (RF) signal (V_g^{AC}) at frequency ω along with a dc voltage (V_g^{DC}) is applied at the gate terminal. Another RF signal (V_s^{AC}) with a slightly

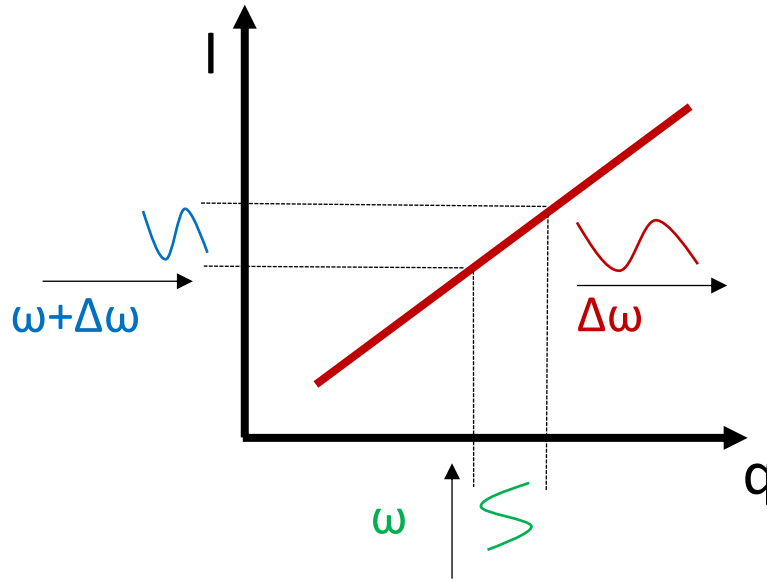


Figure S6: Schematic of the principle of mixed down technique. Modulation of source-drain current and carrier charge density at two different frequencies generates an offset current at $\Delta\omega$.

detuned frequency ($\omega + \Delta\omega$) is applied at the source terminal. Figure S6 shows the principle of frequency mixing technique. Due to the modulation of source-drain current and carrier charge density at two different frequencies ($\omega + \Delta\omega$) and ω respectively, an offset current at frequency of $\Delta\omega$ is generated and can easily be detected through a low frequency lock-in amplifier. The characteristic equation for mixed down current can be formulated in a simple fashion^{5,8}.

The total conductance of the thin membrane under the application of V_g^{AC} at a frequency of ω can be written as

$$G = G^{DC} + \tilde{G} \cos(\omega t) .$$

If a signal at a slightly detuned frequency of $(\omega + \Delta\omega)$, $\tilde{V}_s = V_s^{AC} \cos((\omega + \Delta\omega)t)$ is applied at the source terminal, the source-drain current can be viewed as

$$\begin{aligned}
 I &= G\tilde{V}_s \\
 &= (G^{DC} + \tilde{G} \cos(\omega t))\tilde{V}_s \\
 &= G^{DC}V_s^{AC} \cos((\omega + \Delta\omega)t) + \tilde{G} \cos(\omega t) V_s^{AC} \cos((\omega + \Delta\omega)t) \\
 &= G^{DC}V_s^{AC} \cos((\omega + \Delta\omega)t) + \frac{1}{2}\tilde{G}V_s^{AC} (\cos(2\omega t) + \cos(\Delta\omega t)).
 \end{aligned}$$

So, current through the membrane at the mixed down frequency $\Delta\omega$ is

$$\begin{aligned}
 I_{\text{mix}}^{\Delta\omega} &= \frac{1}{2}\tilde{G}V_s^{AC} \cos(\Delta\omega t) \\
 &= \frac{1}{2} \frac{dG}{dq} \left(V_g^{DC} \frac{dC_g}{dz} z(\omega) + C_g \tilde{V}_g \right) V_s^{AC} \cos(\Delta\omega t).
 \end{aligned}$$

Typically, in the experiments we vary mixed-down frequency from $\sim 1\text{kHz}$ to $\sim 2\text{kHz}$. The second term in the above is the overall background signal attributed to the capacitance between global gate and source-drain contact pads. The background signal can be minimized with a local gate configuration. The first term arises due to mechanical motion of the membrane. Figure S7 shows detailed schematic figure of the two-source mixed down technique implemented in this experiment. This technique has been widely used to characterize CNT and graphene NEMS devices with global back-gate configuration^{5,9-12}.

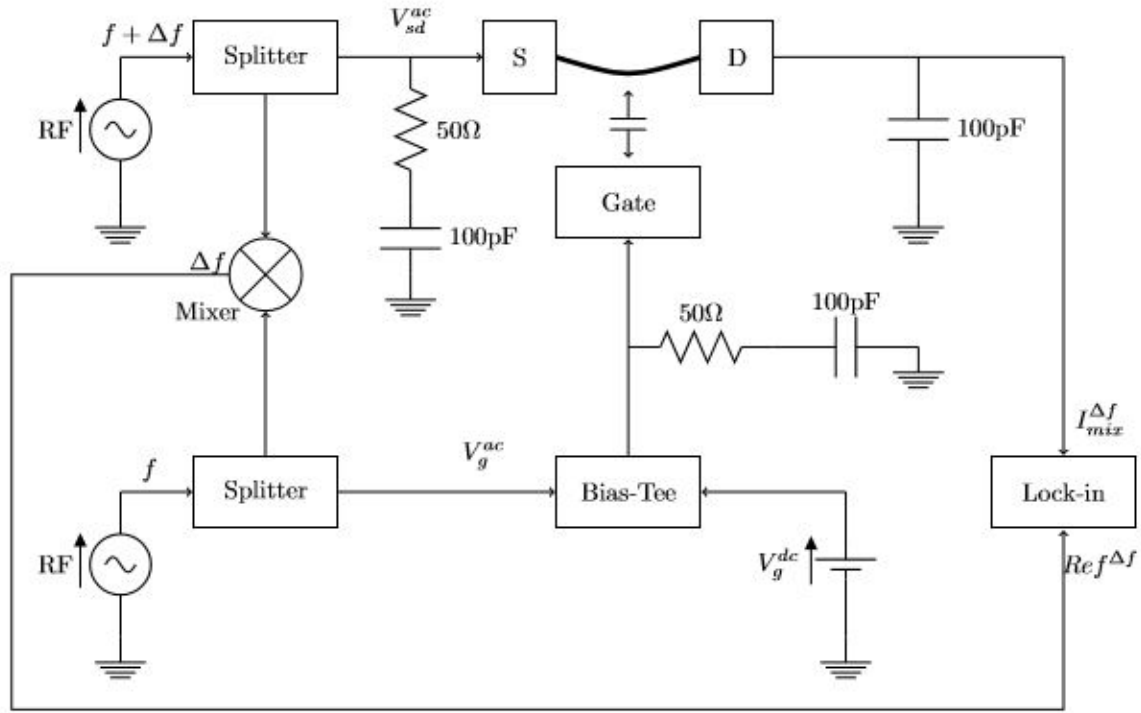


Figure S7: A schematic of two-source heterodyne mixing setup in detail.

Figure S8 shows the frequency response of the fundamental mode obtained using 1ω mixed-down technique for the device. The measured current ($I_{\text{mix}}^{\Delta f}$) in the linear regime is fitted to the following Lorentzian functional form to extract resonant frequency, quality factor, background current ($I_{\text{bg}}^{\Delta f}$) and peak current ($I_{\text{peak}}^{\Delta f}$)⁵.

$$I_{\text{mix}}^{\Delta f} = A + Bf + \frac{H \cos \left(\tan^{-1} \left(\frac{f_0^2 - f^2}{\frac{f_0 f}{Q}} + \Delta\phi \right) \right)}{\sqrt{\left(1 - \left(\frac{f}{f_0} \right)^2 \right)^2 + \left(\frac{f}{Q} \right)^2}},$$

where A , B , H , f_0 , Q and $\Delta\phi$ are independent parameters for the fitting: A and B represent background, H represents the height of the peak current on top of the background, f_0 is the

resonance frequency, Q is the quality factor, and $\Delta\varphi$ is the phase difference due to background current.

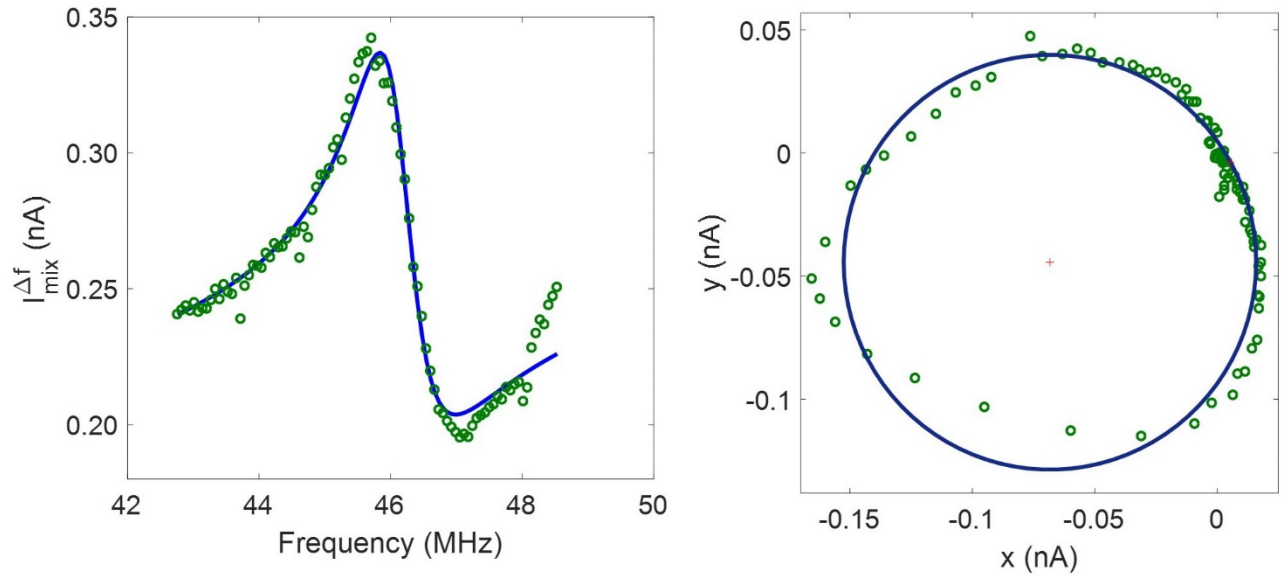


Figure S8: Frequency response of the resonator. The green circles are experimental data and the blue solid lines are the fit to the experimental data.

As we carry out 1ω mixed-down method for the resonance measurement, electrical properties such as conductance, transconductance etc. affect the device readout significantly. Minimum change in electrical properties is desirable to estimate mechanical properties with good accuracy during the measurement. Because of this, we monitor the electrical properties of the resonator at each temperature. Figure S9(a) shows output characteristic of the device at different temperatures. Figure S9(b) shows two-probe conductance values at different temperatures. The conductance values are extracted by linear fitting of the output characteristic. It remains almost constant throughout the range of temperature. Figure S10(a) shows the transfer characteristic,

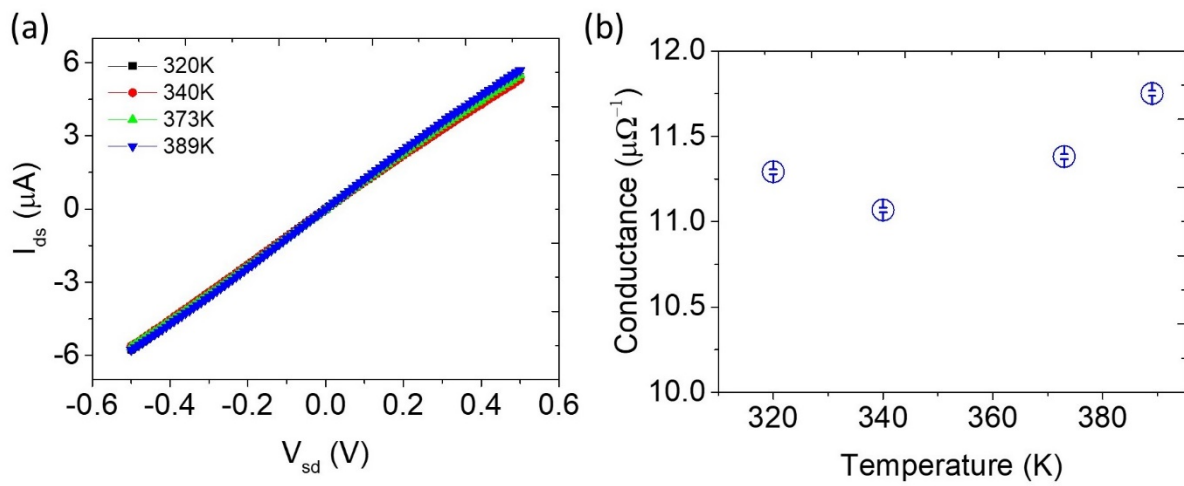


Figure S9: (a) The output characteristics of the device at different temperatures. (b) The two-probe conductance at different temperatures.

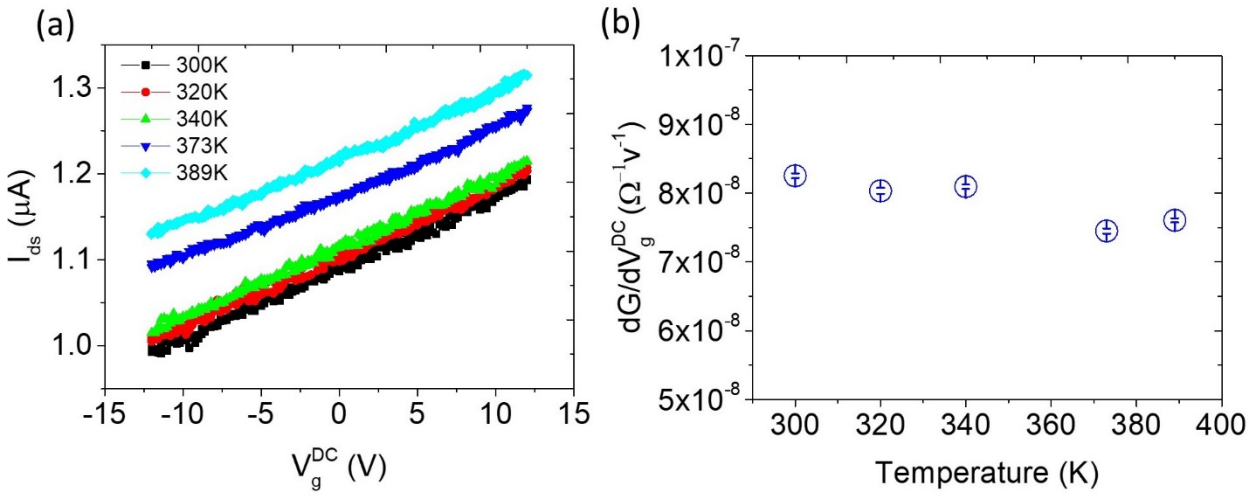


Figure S10: (a) Transfer characteristic of the device at different temperatures while keeping $V_{ds} = 0.1V$. (b) Transconductance at different temperatures.

and figure S10(b) shows the corresponding transconductance of the device at different temperatures. It varies between $8.75 \times 10^{-8} \Omega^{-1}V^{-1}$ to $7.5 \times 10^{-8} \Omega^{-1}V^{-1}$. Thus, electrical

properties of the device remain almost constant throughout the range of temperature during the resonance measurements.

E. Calculation of frequency and nonlinear coefficients:

The equation of motion for our devices can be written as^{8,13}

$$\rho S \frac{d^2 u}{dt^2} + \Gamma \frac{du}{dt} - \left[\epsilon_0 ES + \frac{ES}{2L} \int_0^L \left(\frac{du}{dx} \right)^2 dx \right] \frac{d^2 u}{dx^2} - \frac{1}{2} \frac{dC}{dz} (V_g^{DC})^2 = f_{drive}, \quad (S1)$$

where Γ is the phenomenological linear damping coefficient per unit length, ρ is the three-dimensional mass density, E is Young's modulus, S is the cross-sectional area, L is the length and ϵ_0 is the residual strain of the MoS₂ resonator. Here C is the capacitance per unit length of the resonator and f_{drive} can be written approximately as $\frac{dC}{dz} V_g^{DC} V_g^{AC}$. Here, u is the total displacement of the membrane and can be written as

$$u = z_s(x) + z(x, t), \quad (S2)$$

where $z_s(x)$ is static displacement and $z(x, t)$ is dynamic displacement of the beam. To evaluate the static displacement, we consider the free vibration of the resonator. So, we substitute $f_{drive} = 0$ in equation (S1) and $z(x, t) = 0$ in equation (S2). Then equation (S1) can be reduced as

$$\left[\epsilon_0 ES + \frac{ES}{2L} \int_0^L \left(\frac{dz_s}{dx} \right)^2 dx \right] \frac{d^2 z_s}{dx^2} - \frac{1}{2} \frac{dC}{dz} (V_g^{DC})^2 = 0. \quad (S3)$$

We approximate 1st mode shape¹⁴ of the resonator as

$$\psi(x, t) = \sqrt{2/3} \left[1 - \cos \left(\frac{2\pi x}{L} \right) \right]. \quad (S4)$$

The static displacement can then be written as

$$z_s(x) = A_{dc}\sqrt{2/3} \left[1 - \cos\left(\frac{2\pi x}{L}\right) \right]. \quad (S5)$$

The capacitance per unit length (C) can be expanded as

$$C \approx K_0 + K_1z + K_2z^2 + K_3z^3 + K_4z^4$$

$$\frac{dC}{dz} = K_1 + 2K_2z + 3K_3z^2 + 4K_4z^3, \quad (S6)$$

where $K_1 = -\frac{\epsilon_0 A}{d^2 L}$, $K_2 = \frac{\epsilon_0 A}{d^3 L}$, $K_3 = -\frac{\epsilon_0 A}{d^4 L}$, $K_4 = \frac{\epsilon_0 A}{d^5 L}$, ϵ_0 is the permittivity of free space, A is the area of the resonator, d is the effective air gap between the resonator & gate, and L is the length of the resonator. Incorporating equation (S4), (S5) and (S6) into equation (S3), we obtain

$$\zeta_3 A_{dc}^3 + \zeta_1 A_{dc} + \zeta_0 = 0, \quad (S7)$$

where

$$\zeta_3 = \frac{E}{18} \left(\frac{2\pi}{L}\right)^4 - \frac{35K_4}{9S} (V_g^{DC})^2,$$

$$\zeta_1 = \frac{E\epsilon_0}{18} \left(\frac{2\pi}{L}\right)^4 - \frac{K_2}{S} (V_g^{DC})^2,$$

$$\zeta_0 = -\frac{2K_1}{5S} (V_g^{DC})^2.$$

Expression of static displacement can be derived from equation (S7) as follows.

$$A_{dc} = \frac{\sqrt[3]{\left(\frac{\zeta_0^2}{4\zeta_3^2} + \frac{\zeta_1^3}{27\zeta_3^3}\right)^{0.5} - \frac{\zeta_0}{2\zeta_3}}}{3\zeta_3 \sqrt[3]{\left(\frac{\zeta_0^2}{4\zeta_3^2} + \frac{\zeta_1^3}{27\zeta_3^3}\right)^{0.5} - \frac{\zeta_0}{2\zeta_3}}}. \quad (S8)$$

To determine the resonance frequency and nonlinear coefficient of the resonator, we solve equation (S1) with both static and time varying displacement as described in equation (S2). The time varying displacement can be written as

$$z(x, t) = z(t)\sqrt{2/3}[1 - \cos(2\pi x/L)] \quad (\text{S9})$$

Incorporating equation (S9) and equation (S5) into the equation (S1), the Galerkin discretization procedure¹⁴ gives the time varying part of the equation of motion as

$$\ddot{x} + 2\zeta\dot{x} + \omega_0^2 x + \alpha_2 x^2 + \alpha_3 x^3 = f_{\text{drive}}, \quad (\text{S10})$$

$$\omega_0^2 = \frac{E\epsilon_0}{3\rho} \left(\frac{2\pi}{L}\right)^2 + \frac{EA_{\text{dc}}^2}{6\rho} \left(\frac{2\pi}{L}\right)^4 - \frac{K_2(V_g^{\text{DC}})^2}{\rho S}, \quad (\text{S11})$$

$$\alpha_3 = \frac{E}{18\rho} \left(\frac{2\pi}{L}\right)^4 - \frac{35 K_4 (V_g^{\text{DC}})^2}{9 \rho S}, \quad (\text{S12})$$

$$\alpha_2 = \frac{EA_{\text{dc}}}{6\rho} \left(\frac{2\pi}{L}\right)^4 - \frac{5}{2} \sqrt{\frac{2 K_3 (V_g^{\text{DC}})^2}{\rho S}}. \quad (\text{S13})$$

Incorporating equation (S8) into equation (S11), we get a general expression for the resonance frequency of the resonator. We use this equation to fit experimentally obtained dispersion curves for the devices. Residual strain (ϵ_0) and resonator mass density (ρ) are kept as free parameters to fit the dispersion curves.

F. Estimation of $w_{\text{electrode}}^{\text{total}}$:

It is known that liquid BOE propagates under MoS_2 and etches out the SiO_2 completely under the flake during suspension procedure. To figure out $w_{\text{electrode}}^{\text{total}}$, we dip the device into IPA and then carry out ultrasonication for a long duration to remove suspended part of the electrodes. Figure S6 shows the SEM image of the electrodes after removal of the suspended parts. The maximum value of $w_{\text{electrode}}^{\text{total}}$ can be approximately taken as $0.75\mu\text{m}$. Using equation (2), the

value of $w_{\text{electrode}}^{\text{total}} = 0.75\mu\text{m}$ gives thermal expansion coefficient of single-layer MoS₂ about $\alpha_{\text{MoS}_2} = 2.75 \times 10^{-6}/\text{K}$. It is clear from figure S6 that the actual value of $w_{\text{electrode}}^{\text{total}} = 0.75\mu\text{m}$ is less than $0.75\mu\text{m}$. If we consider $w_{\text{electrode}}^{\text{total}} = 0.50\mu\text{m}$, this result $\alpha_{\text{MoS}_2} = 4.96 \times 10^{-6}/\text{K}$.

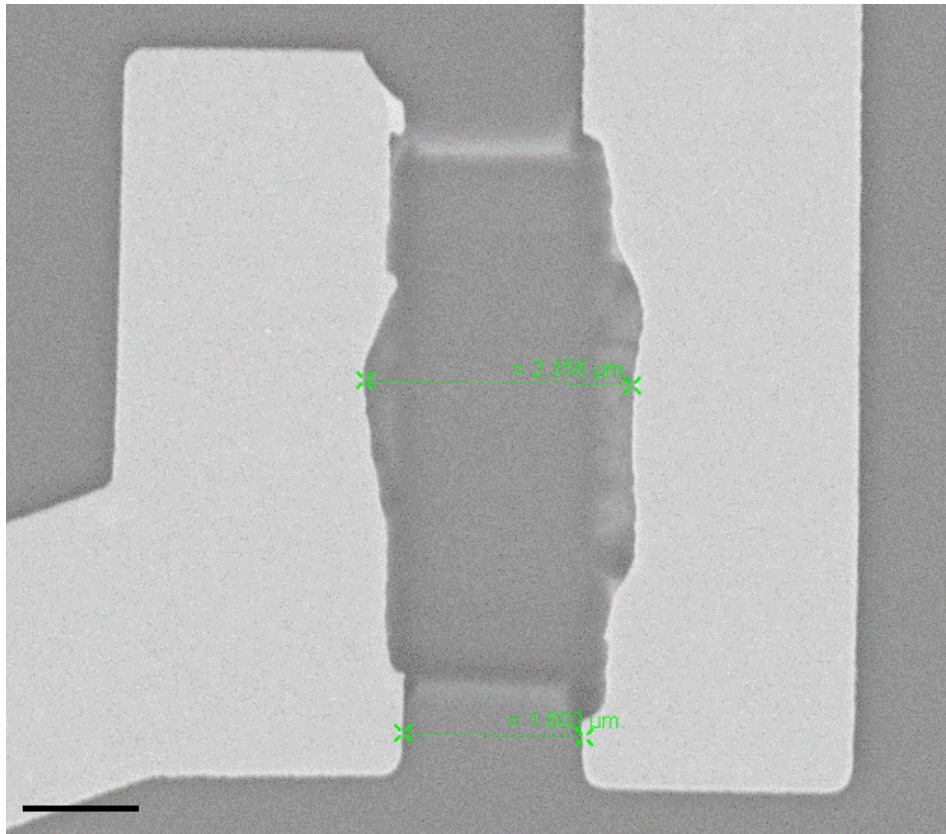


Figure S6: SEM image after removal of MoS₂ flake and suspended part of the electrodes. Scale bar is 1 μm .

G. The device parameters used for the calculations:

Parameters	Values
Young Modulus (E) ^{15,16}	0.3x10 ¹²
Mass density (ρ_0) ¹⁷	5.0x10 ³ Kg/m ³
Length (L)	1.6 μ m
Width (W)	1.0 μ m
Thickness (t)	0.65nm
Mass Loading	3.7 ρ_0
Effective air gap (d)	~185nm
Thermal expansion coefficient of gold (α_{gold})	14.2 x10 ⁻⁶ /K

Table 1: Device parameters used for calculations.

We have used 3D mass density (ρ_0) of monolayer MoS₂ as 5.0x10³ Kg/m³. Thickness (t) of monolayer MoS₂ is 0.65nm. Then, one can easily convert 3D mass density to 2D mass density (ρ_{2D}) as $\rho_{2D} = \rho_0 \times t = 3.25 \times 10^{-6}$ Kg/m².

G. Mechanical characterization of another device fabricated from CVD grown MoS₂:

Figure S7(a) shows SEM image of another device. Figure S7(b) shows amplitude and phase responses in 1 ω mixed-down scheme. Figure S7(c) shows Lorentzian fit to the frequency

response as shown if figure S7(b). Quality factor of the device is about 40. Figure S7(d) shows frequency dispersion of the resonator as a function of V_g^{DC} .

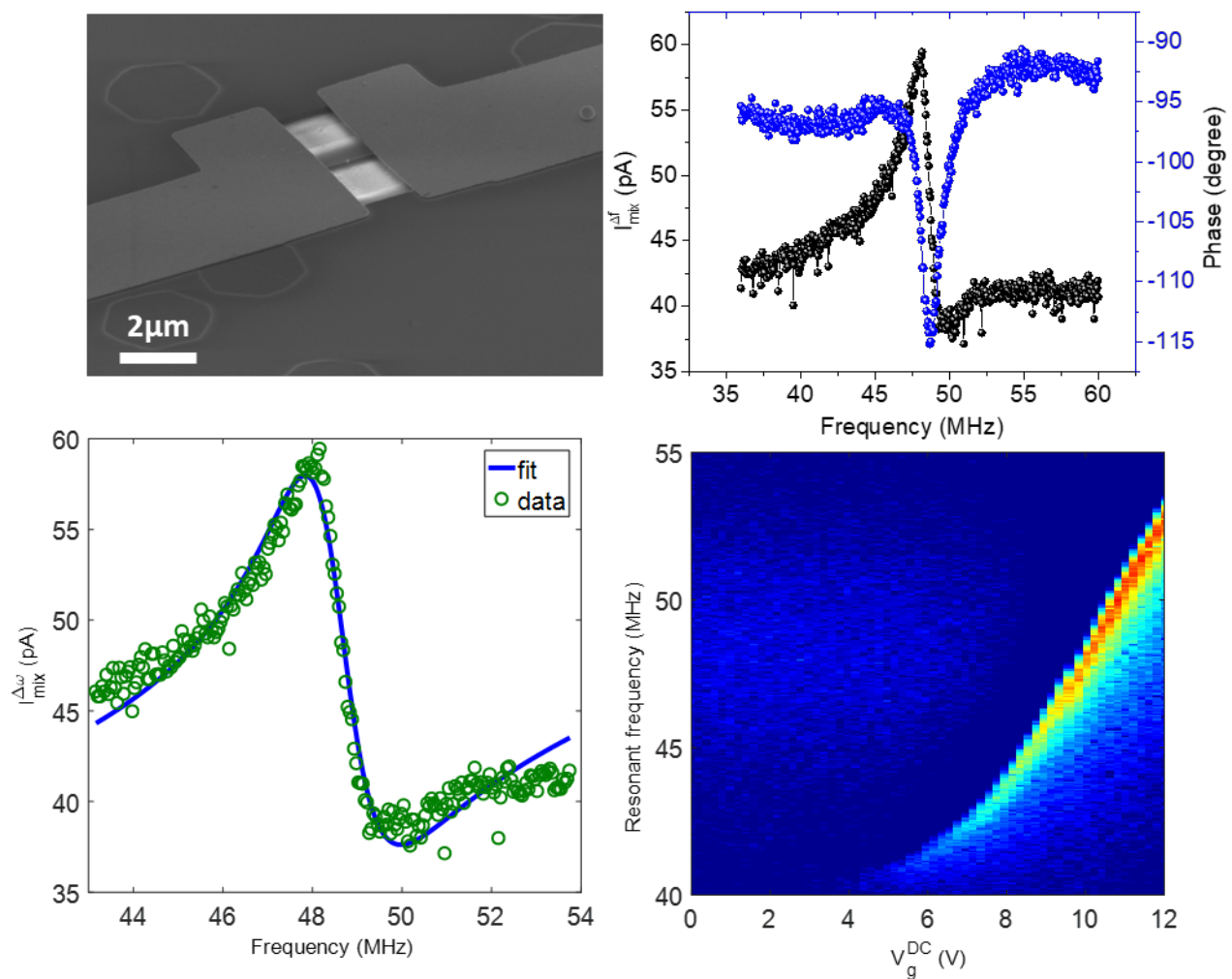


Figure S7: (a) SEM image of another resonator fabricated from CVD grown mono-layer MoS_2 . (b) Amplitude and phase responses of the resonator. (c) Lorentzian fit to the experimental data. Solid blue line is the fit and green circles are data points. (d) Frequency dispersion of the resonator as a function of V_g^{DC} .

References:

1. Kumar, V. K., Dhar, S., Choudhury, T. H., Shivashankar, S. A. & Raghavan, S. A predictive approach to CVD of crystalline layers of TMDs: the case of MoS₂. *Nanoscale* **7**, 7802–7810 (2015).
2. Li, H. *et al.* From Bulk to Monolayer MoS₂: Evolution of Raman Scattering. *Adv. Funct. Mater.* **22**, 1385–1390 (2012).
3. Mouri, S., Miyauchi, Y. & Matsuda, K. Tunable Photoluminescence of Monolayer MoS₂ via Chemical Doping. *Nano Lett.* **13**, 5944–5948 (2013).
4. Tongay, S. *et al.* Broad-Range Modulation of Light Emission in Two-Dimensional Semiconductors by Molecular Physisorption Gating. *Nano Lett.* **13**, 2831–2836 (2013).
5. Sazonova, V. A. A tunable carbon nanotube resonator. (2006).
6. Mathew, J. P., Patel, R. N., Borah, A., Vijay, R. & Deshmukh, M. M. Dynamical strong coupling and parametric amplification of mechanical modes of graphene drums. *Nat. Nanotechnol.* **11**, 747–751 (2016).
7. Chen, C. *et al.* Graphene mechanical oscillators with tunable frequency. *Nat. Nanotechnol.* **8**, 923–927 (2013).

8. Sazonova, V. *et al.* A tunable carbon nanotube electromechanical oscillator. *Nature* **431**, 284–287 (2004).
9. Chen, C. *et al.* Performance of monolayer graphene nanomechanical resonators with electrical readout. *Nat. Nanotechnol.* **4**, 861–867 (2009).
10. Singh, V. *et al.* Probing thermal expansion of graphene and modal dispersion at low-temperature using graphene nanoelectromechanical systems resonators. *Nanotechnology* **21**, 165204 (2010).
11. Zande, A. M. van der *et al.* Large-Scale Arrays of Single-Layer Graphene Resonators. *Nano Lett.* **10**, 4869–4873 (2010).
12. Gouttenoire, V. *et al.* Digital and FM Demodulation of a Doubly Clamped Single-Walled Carbon-Nanotube Oscillator: Towards a Nanotube Cell Phone. *Small* **6**, 1060–1065 (2010).
13. Chen, C. Graphene NanoElectroMechanical Resonators and Oscillators. (2013).
14. Kozinsky, I. Nonlinear nanoelectromechanical systems. (California Institute of Technology, 2007).
15. Castellanos-Gomez, A. *et al.* Elastic Properties of Freely Suspended MoS₂ Nanosheets. *Adv. Mater.* **24**, 772–775
16. Bertolazzi, S., Brivio, J. & Kis, A. Stretching and Breaking of Ultrathin MoS₂. *ACS Nano* **5**, 9703–9709 (2011).
17. Lee, J., Wang, Z., He, K., Shan, J. & Feng, P. X.-L. High Frequency MoS₂ Nanomechanical Resonators. *ACS Nano* **7**, 6086–6091 (2013).

